

See discussions, stats, and author profiles for this publication at: <https://www.researchgate.net/publication/265469032>

# Enhanced Photovoltaic Performance of Polymer Hybrid Nanostructure Heterojunction Solar Cells Based on Poly(3-hexylthiophene)/ZnS/ZnO/Reduced Graphene Oxide Shell–Core Nanorod Arra...

ARTICLE *in* INDUSTRIAL & ENGINEERING CHEMISTRY RESEARCH · AUGUST 2014

Impact Factor: 2.59 · DOI: 10.1021/ie501677r

---

CITATIONS

4

READS

64

## 8 AUTHORS, INCLUDING:



Mehran Sookhakian

University of Malaya

24 PUBLICATIONS 202 CITATIONS

[SEE PROFILE](#)



Yusoff Mohd Amin

University of Malaya

124 PUBLICATIONS 452 CITATIONS

[SEE PROFILE](#)



Rozalina Zakaria

University of Malaya

43 PUBLICATIONS 148 CITATIONS

[SEE PROFILE](#)



Wan Jeffrey Basirun

University of Malaya

172 PUBLICATIONS 738 CITATIONS

[SEE PROFILE](#)

# Enhanced Photovoltaic Performance of Polymer Hybrid Nanostructure Heterojunction Solar Cells Based on Poly(3-hexylthiophene)/ZnS/ZnO/Reduced Graphene Oxide Shell–Core Nanorod Arrays

Mehran Sookhakian,<sup>\*,†</sup> Yusoff Mohd Amin,<sup>†</sup> Rozalina Zakaria,<sup>†,‡</sup> Saeid Baradaran,<sup>||</sup> Mohamad Reza Mahmoudian,<sup>§</sup> Majid Rezayi,<sup>||</sup> Mohamad Taghi Tajabadi,<sup>§</sup> and Wan Jefrey Basirun<sup>§,⊥</sup>

<sup>†</sup>Department of Physics, Faculty of Science, University of Malaya, Kuala Lumpur 50603, Malaysia

<sup>‡</sup>Photonics Research Centre, Faculty of Science, University of Malaya, Kuala Lumpur 50603, Malaysia

<sup>§</sup>Department of Chemistry, Faculty of Science, University of Malaya, Kuala Lumpur 50603, Malaysia

<sup>||</sup>Department of Mechanical Engineering, Faculty of Engineering, University of Malaya, Kuala Lumpur 50603, Malaysia

<sup>⊥</sup>Institute of Nanotechnology & Catalysis Research (NanoCat), University of Malaya, 50603 Kuala Lumpur, Malaysia

**ABSTRACT:** A novel hybrid photoanode based on poly(3-hexylthiophene) (P3HT) modified ZnS/ZnO shell–core nanorod arrays was fabricated on indium tin oxide (ITO) modified reduced graphene oxide (rGO) film using a simple sequential electrodeposition process. The morphology and structure of the as-fabricated electrode were confirmed by X-ray diffraction, field emission electron microscopy, and high-resolution transmission electron microscopy. The electrochemical impedance spectroscopy and current–voltage curve measurements illustrated that the power conversion efficiency of the P3HT/ZnO nanorod arrays electrode was significantly improved by the formation of rGO film and type II band alignment in the heterostructure ZnS/ZnO shell–core nanorod arrays in the four-component P3HT/ZnS/ZnO/rGO electrode. On the basis of these results, P3HT as an excellent hole acceptor, ZnS as an electronic mediator, ZnO as an excellent electron acceptor and direct pathway, and rGO nanosheet as a superior conductive collector and transporter have been shown to have in total a significant effect on increasing photovoltaic efficiency.

## 1. INTRODUCTION

In recent decades, dye-sensitized solar cells based on wide band gap oxide semiconductors and organic or metal–organic complex dyes have been extensively investigated because of their low cost, easy fabrication procedures, and acceptable energy conversion efficiencies compared to those of conventional solid-state silicon-based solar cells.<sup>1</sup> In particular, most attention has focused on the utility of TiO<sub>2</sub> nanostructures as photoelectrodes.<sup>2,3</sup> Besides TiO<sub>2</sub>, new wide band gap oxide semiconductors such as SnO<sub>2</sub>, Nb<sub>2</sub>O<sub>5</sub>, and especially ZnO have been widely used in dye-sensitized solar cell devices.<sup>4–6</sup> ZnO is considered to be the most promising alternative to TiO<sub>2</sub> because ZnO-based photoanodes possess band-gaps and conduction band positions similar to those of TiO<sub>2</sub> photoanodes but with higher electron mobility (ZnO, 115–155 cm<sup>2</sup> V<sup>-1</sup> s<sup>-1</sup>; TiO<sub>2</sub>, 10<sup>-5</sup> cm<sup>2</sup> V<sup>-1</sup> s<sup>-1</sup>)<sup>7</sup> in addition to the ease of crystallization and anisotropic growth.<sup>7</sup> However, there are several problems, such as dye degradation under solar irradiation, the poor stability of ZnO nanostructures in acidic conventional dyes which leads to the formation of Zn<sup>2+</sup>/dye complex, and a relatively nonconductive or insulation layer which generally blocks the overall electron injection efficiency of the dye molecules, which result in the decrease of device conversion efficiency.<sup>8</sup> To overcome these challenges, the substitution for conventional dyes with organic polymers, such as poly(3-hexylthiophene) (P3HT), as excellent electron donor and hole acceptor materials in addition to ZnO nanostructure

as an electron acceptor forms a donor–acceptor interface area for the exciton dissociation and charge generation in polymer-based solar cells (PSCs).

Despite the several advantages of PSCs, such as ease of fabrication and low weight, P3HT/ZnO solar cells still suffer from several problems such as photocorrosion. Fast charge transport rates in semiconductor nanostructures and between semiconductor and conducting electrode are the major challenges. Modification of the semiconductor nanostructure morphology is an efficient strategy for increasing the charge transport rate in semiconductor nanostructures. Aligned one-dimensional (1D) ZnO nanorod arrays are beneficial for increasing the charge transport rate because they can provide a direct electrical channel for photogenerated electron transport.<sup>7</sup> Moreover, the electron transport rate in the crystalline nanorod arrays is expected to be several orders of magnitude faster than percolation through a random polycrystalline network.<sup>7</sup> However, the poor contact between the conducting electrode such as ITO and the ZnO film, as well as the poor conductivity of the ZnO film and the larger interfacial resistance, leads to the accumulation of electrons in the semiconductor layer and a

**Received:** April 23, 2014

**Revised:** August 21, 2014

**Accepted:** August 26, 2014



decrease of charge transfer to the conducting electrode, which results in the low conversion efficiency of the device.

Reduced graphene oxide (rGO), a flat monolayer of  $\text{sp}^2$ -bonded carbon atoms tightly packed into a two-dimensional honeycomb lattice, has attracted tremendous attention because of its properties such as excellent mobility of charge carriers at room temperature ( $200\ 000\ \text{cm}^2\ \text{V}^{-1}\ \text{s}^{-1}$ ), superior electrical conductivity, and high surface area.<sup>9–12</sup> It also demonstrates great promise for the fabrication of solar cell devices.<sup>13</sup> Although rGO has poor photoelectric properties, the formation of heterojunction nanostructures can largely expand, improve, or alter the properties and applications of the pristine rGO. Modification of the conducting electrode by rGO leads to the improvement of conversion efficiency of PSC devices because the high conductivity of rGO makes it a great material for accepting photoinduced charge carriers and promoting the electron transfer rate of the ZnO nanorod arrays conduction band to conducting electrode by trapping the photogenerated electrons.

It must be pointed out that although modification of the conducting electrode by rGO has a promising effect on the increase of charge-transfer rate, the modification of ZnO nanorod array surfaces by inorganic semiconductors is another choice for both impediment of the charge recombination and broadening of the light absorption to the visible region. Surface defects on ZnO nanorod arrays surface will strongly affect the increase of charge recombination of photogenerated electrons by trapping–detraping processes.<sup>14</sup> Therefore, the surface functionalization of ZnO nanorod arrays by narrow band gap inorganic semiconductors such as CdS and CdSe not only will strongly reduce the surface defects resulting from the decrease of recombination rate but also will efficiently decrease the band gap of hybrid-heterojunction structure, which results in more charge generation in the interface.

However, the surface functionalization of wide band gap ZnO nanorod arrays faces some challenges. The narrow band gap semiconductors are sensitive to photodegradation, resulting in the reduction of lifetime of the photodevice.<sup>15</sup> Furthermore, a large number of narrow band gap semiconductors, such as CdS, consist of toxic materials which are unacceptable in certain applications. The hybrid-heterojunction of ZnS and ZnO shell–core nanorod arrays architecture would be an ideal model system for the ZnO surface functionalization for decreasing the threshold energy for charge generation. However, both ZnO and ZnS are wide band gap (ZnO,  $E_g = 3.4\ \text{eV}$ ; ZnS,  $E_g = 3.7\ \text{eV}$ ) semiconductors; the electrons and holes are separated between the core and the shell of the ZnS–ZnO shell–core interface because of the formation of type-II heterostructure band alignment. Thus, the electrons and holes are separated between the core and the shell, giving rise to a significant increase in the injection of photogenerated electrons from ZnS to ZnO and a significant increase in the exciton lifetime. Furthermore, band alignment is favorable for reduction of the photoexcitation threshold energy.

Building from these ideas, we report an electrochemical route for the fabrication of novel P3HT/ZnS/ZnO/rGO shell–core type-II four-component nanorod arrays for the photoanodes of the PSC device. To the best of our knowledge, this is the first demonstration of the functionalization of ZnO/rGO modified indium tin oxide (ITO) electrode surface with ZnS nanoparticles for the fabrication of PSC hybrid solar cells. The easy and low-cost electrodeposition process allows precise control of the several deposited layers without any organic binders and

additives. The designed structure illustrated an overall energy conversion efficiency of up to 1.01% under  $100\ \text{mW cm}^{-2}$  AM 1.5 irradiation, indicating a 2.5-fold improvement in the conversion efficiency compared to that of the P3HT/ZnO photoanode.

## 2. EXPERIMENTAL METHODS

**2.1. Chemical Reagents.** All chemicals were purchased from Merck Co., were of analytical purity, and used without further purification. Milli Q-Plus water (resistance,  $18.3\ \text{M}\Omega$ ) was utilized for all experimental procedures. All experiments were carried out in atmospheric air pressure.

**2.2. Electrochemical Deposition of rGO Film and ZnO Nanorod Arrays.** Micron-sized graphite powder ( $1\text{--}2\ \mu\text{m}$ , Aldrich) was utilized as the initial precursor for the synthesis of graphene oxide (GO) by a modified Hummers method. The electrochemical deposition of the rGO film on the ITO electrode surface was performed using the method reported by Mahmoudian et al.<sup>16</sup> Briefly, the electrochemical deposition of rGO was carried out using a three-electrode electrochemical cell by cyclic voltammetry in one voltammetric cycle. A clean ITO-coated glass substrate was used as the working electrode, while a platinum foil with  $2\ \text{cm}^2$  surface area served as the counter electrode. The solution contained  $7\ \text{mg L}^{-1}$  GO and  $0.1\ \text{M}$  phosphate buffer ( $\text{K}_2\text{HPO}_4$  and  $\text{KH}_2\text{PO}_4$ ) at pH 7.2. The applied potential ranged from  $0.0$  to  $-1.5\ \text{V}$  at a  $1\ \text{mV s}^{-1}$  scan rate with respect to an Ag/AgCl reference electrode.

The electrochemical deposition of ZnO nanorod arrays was performed in a three-electrode electrochemical cell immersed in a water bath held at  $70\ ^\circ\text{C}$ . The fresh rGO modified ITO electrode was used as the working electrode for the nanostructure growth by chrono-amperometry at  $-1.1\ \text{V}$  with respect to an Ag/AgCl reference electrode while a platinum foil served as the counter electrode. The solution contained  $0.001\ \text{M}$   $\text{Zn}(\text{NO}_3)_2$  and  $0.1\ \text{M}$  KCl solution as the supporting electrolyte to increase the conductivity. The deposition time was 45 min. The final product, termed ZG-0, was washed with distilled water and then dried at  $50\ ^\circ\text{C}$  in a conventional oven.

**2.3. Synthesis of ZnS/ZnO/rGO Shell–Core Nanorod Array Electrode.** The ITO-glass substrate with ZnO/rGO nanorod arrays was transferred into a Pyrex glass bottle containing  $0.1\ \text{M}$  thioacetamid (TAA) aqueous solution. The sulfidation process was performed at  $80\ ^\circ\text{C}$  for 1, 3, 5, or 7 h in a conventional oven, and the resulting samples are termed ZG-1, ZG-3, ZG-5, or ZG-7, respectively. Finally, electrodes were washed with distilled water to remove impurities and then dried at  $50\ ^\circ\text{C}$ .

**2.4. Preparation of P3HT Modified ZnS/ZnO/rGO Shell–Core Nanorod Arrays.** A thin layer of P3HT was electrodeposited on top of the as-fabricated ZnS/ZnO/rGO electrode. The electrochemical solution contained  $0.01\ \text{mol L}^{-1}$  tetrabutylammonium tetrafluoroborate and  $0.1\ \text{M}$  3-hexylthiophene in acetonitrile. The ZnS/ZnO/rGO electrodes with different sulfidation times ( $t = 0, 1, 3, 5, 7\ \text{h}$ ) served as the working electrode, a platinum foil as the counter electrode, and an Ag/AgCl as the reference electrode. The applied potential was  $1.9\ \text{V}$ , and the deposition time was 3 min. The as-deposited samples were washed with absolute ethanol and then annealed at  $120\ ^\circ\text{C}$  for 1 h under a nitrogen atmosphere to get a full infiltration of P3HT into the interspaces between nanorods. The samples are termed PZG-0, PZG-1, PZG-3, PZG-5, and PZG-7 for sulfidation times of 0, 1, 3, 5, and 7 h, respectively.

**2.5. Device Fabrication and Photoelectrochemical Measurements.** All working electrodes were prepared by electrochemical deposition. The PSC devices were assembled by working electrodes which consist of P3HT, ZnS, ZnO, and rGO photoanodes; modified ITO films; and a Pt foil as a counter electrode, which was filled with the electrolyte in a 50  $\mu\text{m}$  thick spacer. The  $\text{I}_3^-/\text{I}^-$  liquid electrolyte consists of 0.5 M KI, 0.05 M  $\text{I}_2$ , 0.6 M tetrabutylammonium iodide, and 0.5 M 4-*tert*-butylpyridine in acetonitrile. A PLS-SXE150 halogen lamp (Beijing Perfectlight Technology Corp., China) was utilized as an illumination source. The distance between working electrode and lamp was about 40 cm. The current–voltage ( $I$ – $V$ ) curves and electrochemical impedance spectroscopy (EIS) measurements of the films were performed using a potentiostat–galvanostat (Autolab PGSTAT30) from Ecochemie (Netherlands). The monochromatic incident photon-to-electron conversion efficiency (IPCE) was recorded on a Keithley 2400 sourcemeter under the irradiation of a 150 W tungsten lamp with a 1/4 m double monochromator (Spectral Product DK242).

**2.6. Characterization.** The phase and crystallite size of all shell–core nanorod arrays were characterized using an automated X-ray powder diffraction instrument (XRD; PANalytical Empyrean) with monochromated Cu  $\text{K}\alpha$  radiation ( $\lambda = 1.54056 \text{ \AA}$ ). The particle size and structural characterization of the as-synthesized product were performed using a high-resolution transmission electron microscopy (HRTEM-FEIG-4020, 500 kV) and high-resolution field emission scanning electron microscopy (FESEM; Hitachi SU8000). The samples were ultrasonicated in distilled water before the HRTEM and FESEM characterization. The ultraviolet–visible (UV–vis) absorption spectrum was recorded using an ultraviolet–visible–near-infrared (UV–VIS–NIR) spectrophotometer (Hitachi, U-3500). The photoluminescence (PL) spectra were measured at room temperature by a Hitachi F-5000 system.

### 3. RESULTS AND DISCUSSION

**3.1. Crystalline Structures.** Figure 1a shows the X-ray diffractograms of graphite, GO, and rGO. An intense and sharp diffraction peak for GO appears at  $2\theta = 10.6^\circ$ , which is attributed to the (001) lattice plane corresponding to a *d*-spacing of 0.83 nm, compared to the graphite narrow peak located at  $26.8^\circ$  with an interlayer spacing of 0.33 nm. This is consistent with the lamellar structure of GO.<sup>11</sup> As a comparison, after the electrochemical deposition of GO, the diffractogram illustrates the disappearance of this strong peak and the appearance of a very broad (002) peak at  $2\theta = 23.62^\circ$ , corresponding to a *d*-spacing of 0.38 nm. This suggests that the GO was reduced to rGO sheets during the electrochemical deposition process because of the removal of the functional groups.

The phase structure of the ZnO/rGO nanorod arrays modified ITO electrode and ZnS/ZnO/rGO shell–core nanorod arrays with different sulfidation times are illustrated in Figure 1b. The ZG-0 spectra shows a high-intensity diffraction peak at a  $2\theta$  value of  $34.331^\circ$ , which can be indexed to (002) lattice planes of hexagonal wurtzite ZnO (JCPDS entry 00-001-1136) with the lattice constant  $a = b = 3.24 \text{ \AA}$  and  $c = 5.176 \text{ \AA}$ . Moreover, the high-intensity peak indicates that the hexagonal wurtzite ZnO nanorod arrays are well-crystallized before reacting with the TAA solution and grow preferentially along the *c*-axis with the growth axis parallel to the ITO

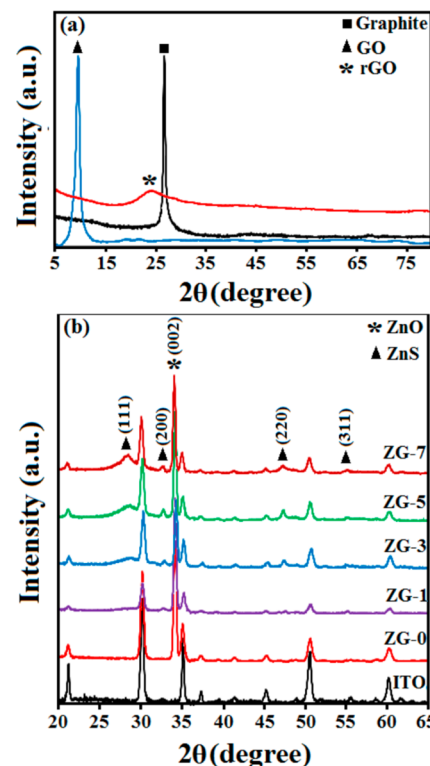


**Figure 1.** (a) XRD patterns of graphite, GO, and rGO. (b) XRD patterns of ITO electrode and ZG- $x$  ( $x = 0, 1, 3, 5, 7$ ) shell–core nanorod arrays with different sulfidation times.

substrate. However, no characteristic diffraction peak of rGO was observed in the ZG-0 film. The typical diffraction peak of rGO was not detected in the ZG-0 film, which can be assigned to the low diffraction peak intensity and low amount of the as-deposited rGO as seen in Figure 1a.<sup>11</sup> When the reaction time is 1 h (ZG-1), the diffraction peak of the ZnO nanorod arrays is still very strong with the appearance of very weak (111), (200), (220), and (311) peaks of sphalerite ZnS (JCPDS entry 00-001-0792). However, as the sulfidation time is increased to 7 h, the intensity peaks corresponding to the cubic ZnS phase are enhanced, indicating that more and more ZnO core was raised into the ZnS shell, as seen in ZG-3, ZG-5, and ZG-7.

**3.2. Morphology and Chemical Composition.** Figure 2a shows the top view of a FESEM image of rGO sheet modified ITO electrode before the deposition of ZnO nanorod arrays. As can be seen, the surface of the rGO thin film is highly smooth while the typical wrinkle-like features are slightly visible. Figure 2b,c illustrates the FESEM images of ZnO nanorod arrays grown on rGO sheet before the formation of ZnS shell. Figure 2b clearly shows the as-deposited ZnO nanorod arrays on rGO modified ITO electrode are vertically aligned, relatively dense, and smooth with a diameter of 20–30 nm and a number density of about  $(4\text{--}5) \times 10^2 \text{ }\mu\text{m}^{-2}$ . The high-magnification FESEM image clearly reveals that the ZnO nanorod arrays are well-distributed on the rGO surface and that the rGO nanosheets can also function as conductive bands for the interconnection between the various ZnO nanorod arrays and ITO electrode to transfer the photogenerated charge carriers for the enhancement of the photocurrent effect (Figure 2c).

Moreover, the inset of Figure 2c shows the cross-sectional view of the ZnO nanorod arrays. As can be seen, the nanorods are well-aligned with an average length of  $\sim 150 \text{ nm}$ , and the

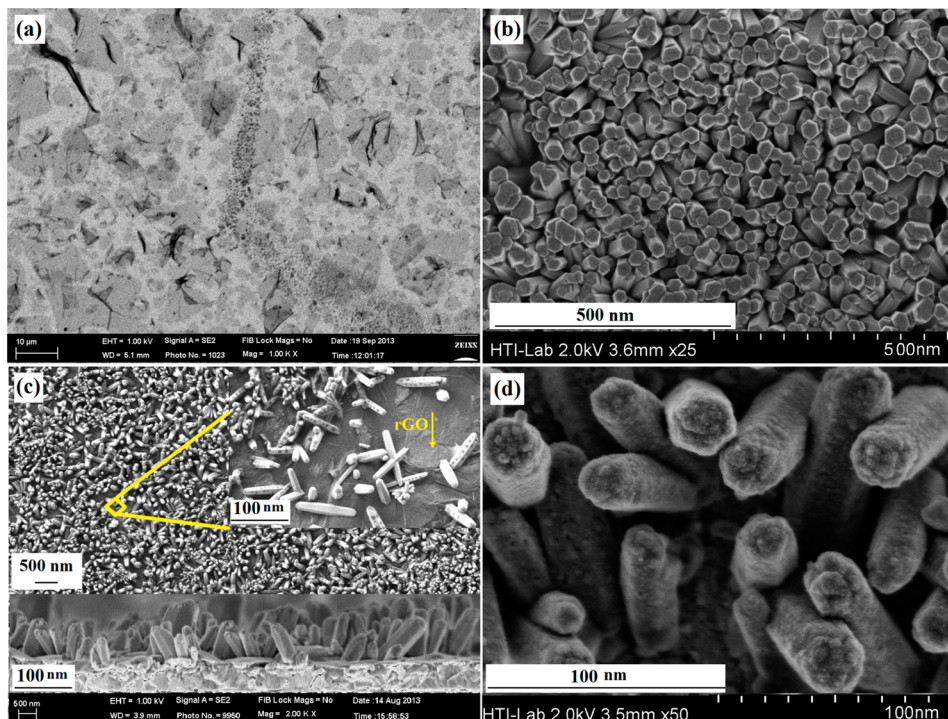


**Figure 2.** (a) FESEM image of graphene nanosheets on ITO substrate; (b) top view FESEM image of ZnO-rGO electrode; (c) low-magnification FESEM image of ZnO-rGO, inset clearly showing the formation of ZnO nanorod on rGO and the cross section FESEM image of ZnO nanorod arrays; (d) high-magnification FESEM of ZnS-ZnO core–shell nanorod arrays.

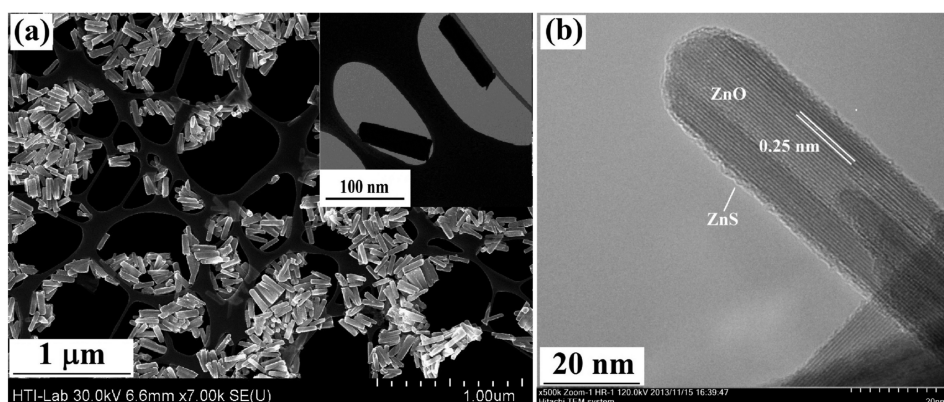


**Figure 3.** (a) TEM image of ZnO nanorod arrays. The inset is a high-magnification TEM image of ZnO nanorod arrays. (b) High-resolution transmission microscopy image of ZnS/ZnO core-shell.

nанороды стоят вертикально под углом 20° к подложке. После формирования ZnS на поверхности ZnO нанородов, морфология чистых ZnO нанородов не изменилась, но поверхность нанородов стала шероховатой и диаметры значительно увеличились, как можно увидеть на рисунке 2д для ZG-7.

Further investigation of the crystal structure was performed by TEM and HRTEM techniques. Figure 3a shows the TEM image of initial ZnO nanorod arrays, where the as-electro-chemically prepared ZnO nanorods appear to be smooth on the surface (the inset of Figure 3a). The HRTEM image of ZnS/ZnO shell–core nanorod arrays after a 5 h sulfidation process is shown in Figure 3b. As seen, the apparent contrast between the inner core and the outer shell reveals the existence of a shell–core structure. The ZnS shell with an estimated thickness of 6 nm is clearly observed, which implies that the encapsulation of ZnO by ZnS was successfully. The lattice fringes of 0.25 nm in

the core region corresponding to the (002) crystal planes of wurtzite ZnO is confirmed by high-magnification HRTEM analysis. However, the crystallinity of the ZnS shell is rather poor because of the ZnS shell formation at low temperature. Moreover, the connection between the ZnS shell and the ZnO core are strong, and ZnS layers could not be detached from the ZnO core even after ultrasonic washing.

**3.3. Optical Properties.** Figure 4 shows the comparison of UV-vis spectra of pure ZnO and ZG- $x$  thin film electrode ( $x = 0, 1, 3, 5$  and  $7$ ). As can be seen in Figure 4, the electrochemical deposition of pure ZnO nanorod arrays on the ITO electrode causes an obvious excitonic absorption peak in the UV region with a band gap absorption edge at  $388$  nm. Compared to pure ZnO nanorod, the ZG-0 electrode shows a gradual increase of absorption in the visible region between  $400$  to  $550$  nm because of the presence of rGO.

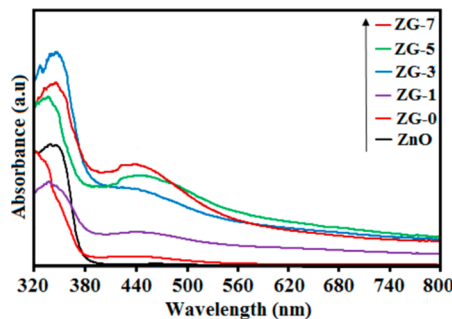


**Figure 4.** UV–vis absorption spectra of pure ZnO and ZG- $x$  ( $x = 0, 3, 5, 7$ ).

After the formation of ZnS nanoparticles on the ZnO nanorod surface, the ZG- $x$  shell–core nanorod arrays extend their optical absorption in the visible region and the absorption edge shifts toward longer wavelength up to 450 nm, which is red-shifted compared to that of the ZG-0. Moreover, the visible light absorption in the visible region gradually increases with the increase of the sulfidation time up to 7 h because of the increased amount of ZnS nanoparticles. Photoluminescence measurements were performed to investigate the effect of ZnS shell on the ZnO core for the charge-transfer process. As seen in Figure 5, the two typically sharp and broad peaks of pure

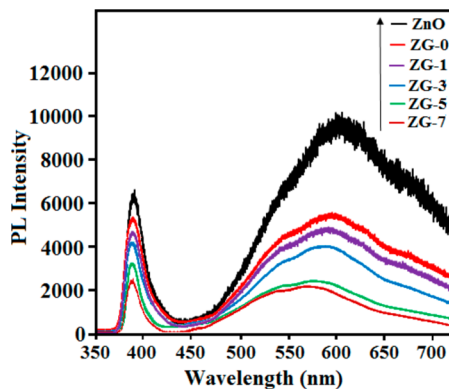


**Figure 5.** Photoluminescence spectra of pure ZnO and ZG- $x$  ( $x = 0, 1, 3, 5, 7$ ).

ZnO nanorod arrays can be found at 384 and 565 nm, corresponding to the near band edge (NE) emission and deep level emission (DE), respectively. The NE emission originates from the recombination of free excitons in the near band edge of the wide band gap ZnO nanorod arrays, and the DE emission is assigned to various intraband defects in the crystal, such as zinc vacancy, zinc interstitial, oxygen vacancy, oxygen interstitial, and oxygen antisite.<sup>17</sup>

Compared to that of the pure ZnO nanorod arrays, the PL spectra of ZG- $x$  shell–core are approximately similar to the pure ZnO but are quenched in the ZG- $x$  shell–core. In these systems, because of the presence of a type II band alignment, one carrier is mostly confined to the core, while the other is mostly confined to the shell. Therefore, the energy gradient at the interfaces tends to spatially separate the electrons and holes on different sides of the heterojunction.<sup>18</sup> Furthermore, the emission peaks of ZnS are not observed, indicating an effective formation of type II band alignment between ZnO nanorods and ZnS shell resulting in effective electron transfer from the conduction band of the ZnS shell to the ZnO core. Moreover,

when the sulfidation time is increased from 1 to 7 h, both NE and DE peaks of ZG- $x$  ( $x = 1, 3, 5, 7$ ) are slightly shifted to shorter wavelength, which is blue-shifted as compared to that of the ZG-0; in addition, the DE peaks are significantly quenched up to 5 h. However, the DE intensity is only decreased weakly for 7 h. It is well-known that the intensity ratio of DE to NE ( $I_{\text{DE}}/I_{\text{NE}}$ ) is related to the density of surface defects in the semiconductor band gap which is used to indicate the crystal quality. Compared to that of the pure ZnO nanorod, the  $I_{\text{DE}}/I_{\text{NE}}$  mratio of ZG- $x$  decreased from 1.32 to 0.38 with the increase of sulfidation time in the range of  $t = 1–5$  h because of decrease in the surface defects of the ZnO nanorod arrays. However, the further increase of sulfidation time from 5 to 7 h did not alter remarkably the  $I_{\text{DE}}/I_{\text{NE}}$  ratio. According to the mechanism of growth, the possible process for the reduction of surface defects of the ZnO nanorod core with the formation of ZnS shell can be predicted. During the sulfidation reaction of ZnO nanorod arrays in TAA, the S<sup>2-</sup> anions released from the decomposition of TAA are easily captured by oxygen vacancies because of the similar chemical properties of sulfur and oxygen atoms.<sup>19</sup> The S<sup>2-</sup> anions then react with the Zn<sup>2+</sup> from the surface of the ZnO nanorod to provide the initial ZnS nucleation around the ZnO core, which will lead to decreased surface defects on the ZnO nanorods from the ZnS growth. Therefore, the sulfidation time dependence of intensity ratios and the shift of emission peak position illustrate that the formation of the ZnS shell up to  $t = 5$  h significantly passivates the ZnO surface states to the largest extent, resulting in the decrease of recombination charge carriers.

Figure 6 shows room-temperature PL spectra of the PZG- $x$  shell–core nanorod arrays ( $x = 1, 3, 5, 7$ ) in the presence of

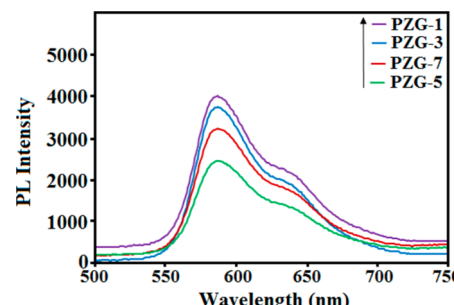


**Figure 6.** Photoluminescence spectra of PZG- $x$  ( $x = 1, 3, 5, 7$ ) in the presence of P3HT.

P3HT after thermal annealing. As can be seen, the PL spectra of all electrodes are similar to that of the pure P3HT; however, the presence of ZnO and ZnS in the system causes quenching in the PL spectra of the pure P3HT, indicating that an effective exciton dissociation at the P3HT/ZnO interface leads to efficient charge transfer at the interface. Moreover, with ZnS shell formation, the quenched polymer PL emission of PZG- $x$  initially increases for PZG-1, PZG-3, and PZG-5 because of the increase of sulfidation time up to 5 h, which leads to the diameter enhancement of the ZnS/ZnO shell–core nanorod arrays, resulting in the enlarged interface area between the polymer and ZnS/ZnO shell–core nanorod arrays for the exciton dissociation.

However, further increase in the sulfidation time up to 7 h leads to the decrease for the quenched P3HT polymer PL emission. This is because the further decrease of polymer amount between the shell–core nanorod arrays due to further

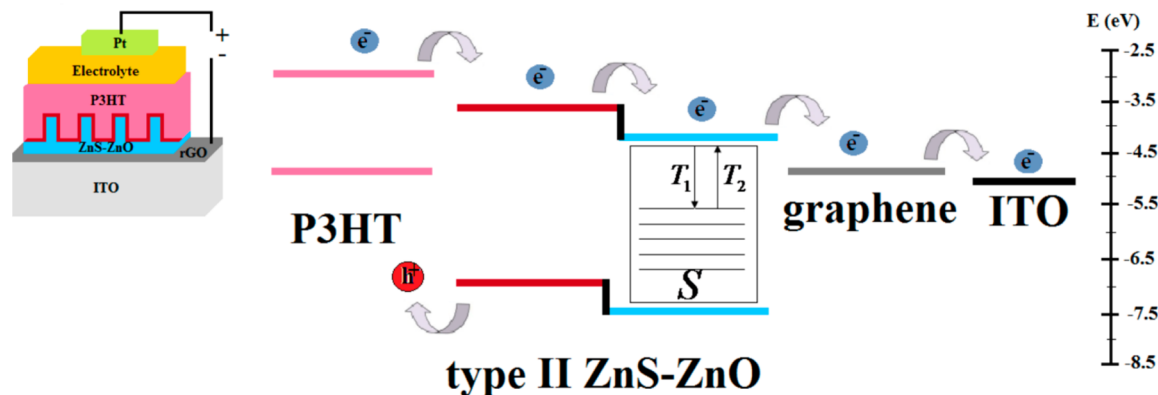


**Figure 7.** Schematic representation of the solar cell device based on the four-component PZG- $x$  shell–core nanorod arrays on ITO substrate and the mechanism of the photocurrent generation.

increase of diameter of nanorods leads to the relaxation of polymer excitons to the ground state by radiative decay before reaching the interface within their lifetimes.

**3.4. Photoelectrochemical Performance.** A schematic of the solar cell device fabricated with the P3HT/ZnO/rGO shell–core nanorod arrays modified ITO electrode is illustrated in Figure 7. To investigate the influence of rGO and ZnS shell on the photoelectrochemical conversion efficiency of the solar cell devices, the current–voltage curve measurements of the device fabricated with P3HT/ZnO nanorod arrays, termed P-ZnO and PZG- $x$  ( $x = 0, 1, 3, 5$  and  $7$ ) modified ITO electrodes, have been performed under  $100 \text{ mW cm}^{-2}$  light illumination at room temperature, as illustrated in Figure 8.

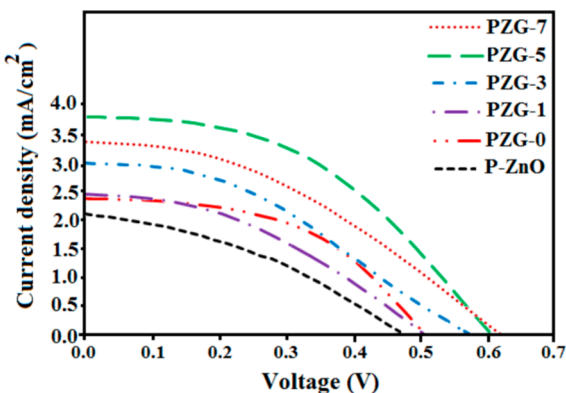


**Figure 8.**  $I$ – $V$  curves of P3HT/ZnO and PZG- $x$  solar cell devices.

Furthermore, Table 1 summarizes the photoelectrochemical parameters of the electrodes. As seen in Figure 8, the presence of rGO and ZnS shell leads to the enhancement of conversion efficiency of P3HT/ZnO and P3HT/ZnO/rGo from 0.39% to

**Table 1. Photovoltaic Properties of the PSC Devices Based on Different Photoanodes**

sample	$V_{oc}$ (V)	$J_{sc}$ ( $\text{mA cm}^{-2}$ )	ff	$\eta$ (%)
P-ZnO	0.48	2.18	0.38	0.39
PZG-0	0.51	2.34	0.40	0.48
PZG-1	0.52	2.47	0.40	0.52
PZG-3	0.58	3.16	0.43	0.78
PZG-5	0.61	3.86	0.43	1.01
PZG-7	0.62	3.41	0.43	0.90

0.48% and 0.48% to 1.01%, respectively. However, with the increase of the sulfidation time up to 5 h, the  $J_{sc}$  initially increases from  $2.47 \text{ mA cm}^{-2}$  for PZG-1 to  $3.86 \text{ mA cm}^{-2}$  for PZG-5, but further increase in sulfidation time up to 7 h leads to a decrease in  $J_{sc}$ . Optimized conversion efficiency is obtained from PZG-5 (based on P3HT/ZnS ( $t = 5 \text{ h}$ )/ZnO/rGO shell–core nanorod array electrode), with  $\eta = 1.01\%$  under AM 1.5 illumination ( $100 \text{ mW cm}^{-2}$ ), which is ca. 2-fold higher than that of the PZG-0 electrode.

It is noteworthy that the reasons for the enhanced efficiency of PZG- $x$  ( $x = 1, 3, 5, 7$ ) electrode in the presence of the ZnS shell compared with the PZG-0 electrode in the absence of the ZnS shell could be attributed to three factors: (i) the increase in charge generation, (ii) decrease in surface defect states of ZnO surface, and (iii) providing the electronic mediator by ZnS for the energy levels construction in the PZG- $x$  shell–core nanorod array devices. In the PSC devices, two crucial factors such as the exciton generation and dissociation play important roles in increasing the efficiency of the solar cell devices. The contribution of the P3HT polymer in exciton generation is dominantly higher than that of the ZnO nanorod arrays because of the wider band gap of the ZnO nanorod arrays compared to that of the P3HT, which results in a greater decrease in light absorption. Therefore, the charge generation in P3HT/ZnO nanorod arrays correlates with the P3HT excitons generated in the interspace between ZnO nanorod arrays, while exciton dissociation dominantly correlates with the interface between P3HT and ZnO side face with a length around 150 nm, as shown in Figure 2c. However, with the formation of the ZnS shell, the contribution of ZnS/ZnO shell–core nanorod arrays for the generation of the photo-generated charge carriers is increased compared to that of the P3HT because of the requirement for additional absorption of the exciton generation, as seen in Figure 4. Therefore, both P3HT and ZnS/ZnO shell–core nanorod arrays actively contribute to the charge generation, resulting in the further increase in the conversion efficiency of the solar cell devices. The second reason for the efficiency enhancement of the PZG- $x$  four-component solar cell devices in the presence of ZnS is the reduction of surface defects of the ZnO surface. Indeed, the surface defects in the ZnO nanorod array strongly affect the decrease of exciton dissociation resulting in the fast recombination kinetics of photogenerated electrons by the trapping–detrapping process. As seen in Figure 7, the photogenerated electrons injected into the conduction band of ZnO may be trapped ( $T_1$ ) by surface defect states of ZnO

surface (S region) and the trapped electrons can be thermally released ( $T_2$ ) into the conduction band; therefore, the photogenerated electrons will not be able to easily escape from the P3HT/ZnO interface because of the presence of a large number of holes in surface states of the ZnO nanorod arrays. However, the existence of the ZnS shell leads to the decrease of defect states on the ZnO surface, as shown in Figure 5. After the sulfidation process, a substantial number of defect states of the ZnO surface will be filled with the formation of the ZnS shell, resulting in the decrease of charge recombination and increase of conversion efficiency of the device.

To understand better the mechanism of electron transfer in the PZG- $\alpha$  shell–core nanorod array electrode, Figure 7 presents the electron-transfer process scheme between the P3HT, ZnS, ZnO, and rGO after being excited by light. As seen in Figure 7, the energy level structure of the electrodes is changed and stepwise energy levels are formed after the formation of the PZG- $\alpha$  electrode. In such a scheme, the visible light is absorbed by the P3HT and ZnS/ZnO shell–core nanorod arrays and the electron–hole pairs are generated. From the electronic structures of P3HT and ZnS, a p–n junction is formed on the interface between the p-type P3HT and the n-type ZnS, resulting in the separation of the photogenerated charge carriers in the interface. The separated electrons are efficiently transferred from the conduction band of the ZnS shell to the conduction band of the ZnO core and then quickly transferred to the rGO and then to the ITO substrate, along the direct path of the ZnO nanorod arrays. Meanwhile, the separated holes are transferred to P3HT via ZnS and scavenged by the  $I_3^-/I^-$  couple in the electrolyte. Therefore, ZnS serves not only as the photosensitizer but also the electronic mediator, which significantly improves the  $J_{sc}$  and the conversion efficiency of the PZG- $\alpha$  devices.

However, the conversion efficiency and  $J_{sc}$  of the PSC devices are a function of sulfidation times, as can be seen in Figure 8 and Table 1. To better explain the details of this mechanism, Figure 9 illustrates the effect of ZnS shell on the  $J_{sc}$  of the

dissociate, as seen in Figure 9. However, along with the formation of the ZnS shell with the thickness of  $R_s$ , a new ineffective region will also be presented for  $R_s + R_d \leq R_i/2$  decreases ( $X'_{if} < X_{if}$ ). However, this reduction cannot affect the population of the effective excitons in P3HT for charge generation because the amount of reduction of P3HT between the ZnS/ZnO/rGO nanorod arrays in the range of  $R_s + R_d \leq R_i/2$  leads to the production decrease of the inefficient excitons, and production of efficient excitons remains constant.

On the other hand, with the increase in sulfidation time which results in the enhancement of ZnS shell thickness, the absorption of ZnS/ZnO shell–core nanorod arrays significantly increases (Figure 4). Therefore, the contribution of ZnS/ZnO shell–core nanorod arrays in charge generation significantly enhances without a remarkable influence on P3HT contribution, which leads to the enhancement of  $J_{sc}$  and conversion efficiency of the PZG-1, PZG-3, and PZG-5, as seen in Table 1. However, a further increase of sulfidation time to 7 h leads to further increase in shell thickness to  $R_s + R_d > R_i/2$  and further decrease in the amount of P3HT between the ZnS/ZnO/rGO nanorod arrays, which results in a decrease of effective excitons in the polymer. Therefore, in the range of  $R_s + R_d > R_i/2$ , the decreased P3HT contribution to charge generation will be in competition with the increased ZnS/ZnO contribution to exciton generation. However, due to the higher amount of absorption coefficient of P3HT ( $\alpha = 10^5 \text{ cm}^{-1}$ )<sup>21</sup> compared to that of ZnS and ZnO [ $\alpha = 10^4 \text{ cm}^{-1}$ ]<sup>22,23</sup> the decreased P3HT contribution will inevitably suppress the increased ZnS/ZnO contribution for charge generation, resulting in the decrease of conversion efficiency and  $J_{sc}$  of the PZG-7 device. Therefore, P3HT absorption still dominantly governs the charge generation in P3HT/ZnS/ZnO/rGO nanorod arrays devices, but ZnS/ZnO shell–core has an effect on the exciton generation by providing more absorption and reduction of the P3HT contribution.

However, the conversion efficiency and  $J_{sc}$  of P-ZnO in the presence of rGO increases from 0.39% and  $2.18 \text{ mA cm}^{-2}$  to 0.48% and  $2.34 \text{ mA cm}^{-2}$ , respectively, for PZG-0. The efficiency enhancement in the presence of rGO correlates with several parameters such as higher electrical resistance of the rGO-modified ITO electrode compared to that of the bare ITO electrode, enhancement of electronic detrapping, and inhibition of fast charge recombination due to its excellent conductivity and rapid transport of photogenerated electrons. To further investigate the effect of rGO on photovoltaic performance of PZG- $\alpha$  devices, an impedance analysis of the PZG-5 without rGO (termed PZ-5) was performed under illumination by applying a 10 mV AC signal over a frequency range of  $1\text{--}10^5 \text{ Hz}$ , and results are illustrated in Figure 10. The EIS Nyquist plots of the PSC devices illustrate a high-frequency response due to the electrochemical reaction and charge transfer at the Pt counter electrode–electrolyte interface, which is the reduction of  $I_3^-$  to  $I^-$  at the CE interface, as well the intermediate frequency response which is associated with the charge transfer and recombination at the P3HT/ZnS/ZnO/rGO interfaces. Finally, the low-frequency response is ascribed to the Warburg diffusion process of  $I_3^-/I^-$  in the electrolyte. The semicircle with a larger diameter represents the larger interfacial resistance and higher interfacial charge recombination in the interfaces. As can be seen in Figure 10, the diameters decrease in the presence of rGO in the PZG-5 compared to that of the PZ-5, which suggests that the presence of rGO leads

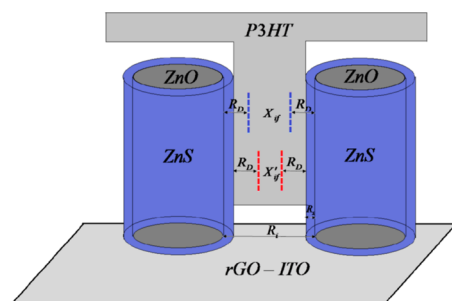


**Figure 9.** Schematic illustration of the effect of ZnS shell thickness on power conversion efficiency of solar cell devices.

devices. As seen in Figure 9, the average diameter of the ZnO nanorod arrays is about 20 nm and the average interspacing ( $R_i$ ) between the nanorod arrays is about 12 nm. However, the exciton diffusion length ( $R_d$ ) of P3HT is very short (3–8 nm);<sup>20</sup> therefore, only excitons within the range of exciton diffusion length of P3HT have a real chance of reaching the P3HT/ZnO interface for exciton dissociation and photo-generated electron production. Because  $R_d < R_i/2$ , there exists a region in the P3HT ( $X'_{if}$ ) where the excitons are ineffectively slow and cannot reach the interface within their lifetime to

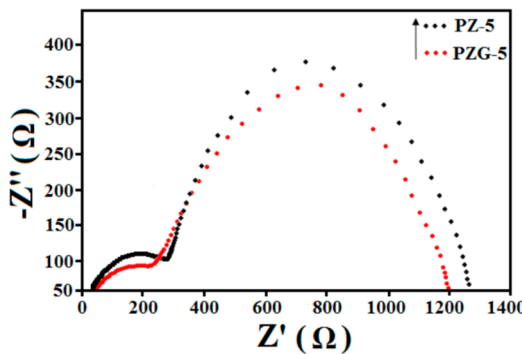


**Figure 10.** EIS Nyquist plots of PSC devices based on the P3HT/ZnS/ZnO and P3HT/ZnS/ZnO/rGO.

to the reduction of charge-transfer resistance and charge recombination at the ZnO–ITO–electrolyte interface.

The enhanced cell performance of ZnO nanorod arrays photoanode in the presence of P3HT, ZnS shell, and rGO is confirmed by an incident photon-to-current efficiency measurement as a function of wavelength (Figure 11). The IPCE is

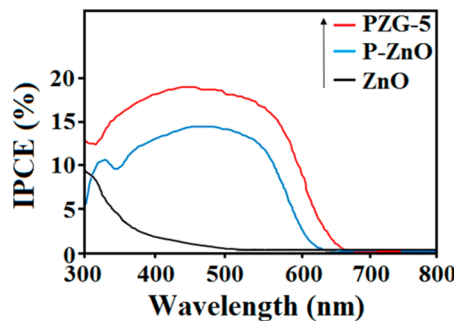


**Figure 11.** Incident photon-to-current conversion efficiency (IPCE) curves of the photoanodes based on ZnO, P3HT/ZnO nanorod arrays, and P3HT/ZnS(Sh)/ZnO shell–core nanorod arrays.

measured by the light absorption efficiency of the sensitizers, the quantum yield of electron injection in the interfaces, and the efficiency of collecting the injected electrons at the ITO substrate. Compared with that of the photoanode based on the ZnO nanorod arrays, P3HT/ZnO photoanode shows a sharp increase of the IPCE in the visible region, probably attributed to the formation of  $Zn^{2+}$ /dye complexes on the surface of the ZnO nanorod arrays in the absence of P3HT and enhanced electron injection caused by the P3HT layer. After the formation of the ZnS shell and rGO, the IPCE of the PZG-5 shell–core nanorod array photoanode reveals a further enhancement. These results show that the formation of the ZnS shell and rGO can effectively increase the electron injection rate and charge transport in the designed photoanode.

It is worth mentioning that although the efficiency of the present PSC device is not very high, our results illustrate that environmentally friendly PSCs can potentially be harnessed as a replacement for toxic semiconductors and provide the advantage of hole transport for the next generation of PSC devices by further optimizing the device configuration.

#### 4. CONCLUSION

rGO nanosheet and ZnO nanorod arrays with average length of 150 nm, diameter of 20 nm, and number density of  $(4\text{--}5) \times 10^2 \mu\text{m}^{-2}$  were grown on an ITO substrate by an electro-

deposition method. ZnS/ZnO/rGO shell–core nanorod arrays have been successfully synthesized by low-temperature hydrothermal growth through the reaction of ZnO/rGO nanorod arrays and TAA, followed by the P3HT electrodeposition. Novel four-component P3HT/ZnS/ZnO/rGO shell–core nanorod array electrodes with different sulfidation times were used as the photoanode in the PSC devices. The current–voltage curve measurements illustrate that (i) the presence of the ZnS shell and rGO nanosheet lead to a 2.5-fold improvement in power conversion efficiency of the PSC devices because of the increase in absorption range for charge generation, decrease in surface defect states of ZnO surfaces and reduction of exciton recombination rate; (ii) the power conversion efficiency of PSC devices as a function of sulfidation time and maximum conversion efficiency of 1.01% was obtained by optimization of the sulfidation time to 5 h for P3HT/ZnS(Sh)/ZnO/rGO shell–core nanorod array; (iii) further increase in sulfidation time up to 7 h leads to a decrease in conversion efficiency of the PSC device because of a decrease in contribution of P3HT to charge generation. Moreover, EIS measurements illustrated that rGO not only decreased the electrolyte–electrode interfacial resistance and exciton recombination rate but also increased the charge transport from the ZnO nanorod arrays to the ITO substrate.<sup>24,25</sup>

#### AUTHOR INFORMATION

##### Corresponding Author

\*Tel/Fax: +603-79675330. E-mail: m.sokhakian@gmail.com.

##### Notes

The authors declare no competing financial interest.

#### ACKNOWLEDGMENTS

The authors thank MOHE and University of Malaya for providing financial assistance with Grants PV136-2012A, RP008E-13AET, FP033 2013, and UM.C/625/1/HIR/MOHE/SCI/29 for this work.

#### REFERENCES

- O'Regan, B.; Grätzel, M. A low-cost, high-efficiency solar cell based on dye-sensitized colloidal  $TiO_2$  films. *Nature (London, U.K.)* **1991**, *353*, 737–740.
- Grätzel, M. Photoelectrochemical cells. *Nature (London, U.K.)* **2001**, *414*, 338–344.
- Green, M. A.; Emery, K.; King, D. L.; Hishikawa, Y.; Warta, W. Solar cell efficiency tables (version 28). *Prog. Photovoltaics* **2006**, *14*, 455–461.
- Sayama, K.; Sugihara, H.; Arakawa, H. Photoelectrochemical properties of a porous  $Nb_2O_5$  electrode sensitized by a ruthenium dye. *Chem. Mater.* **1998**, *10*, 3825–3832.
- Ferrere, S.; Zaban, A.; Gregg, B. A. Dye sensitization of nanocrystalline tin oxide by perylene derivatives. *J. Phys. Chem. B* **1997**, *101*, 4490–4493.
- Keis, K.; Lindgren, J.; Lindquist, S.-E.; Hagfeldt, A. Studies of the adsorption process of Ru complexes in nanoporous ZnO electrodes. *Langmuir* **2000**, *16*, 4688–4694.
- Guerguerian, G.; Elhordoy, F.; Pereyra, C. J.; Marotti, R. E.; Martín, F.; Leinen, D.; Ramos-Barrado, J. R.; Dalchiele, E. A. ZnO nanorod/CdS nanocrystal core/shell-type heterostructures for solar cell applications. *Nanotechnology* **2011**, *22*, 505401.
- Ganesh, T.; Mane, R. S.; Cai, G.; Chang, J. H.; Han, S. H. ZnO nanoparticles–CdS quantum dots/N3 dye molecules: Dual photosensitization. *J. Phys. Chem. C* **2009**, *113*, 7666–7669.
- Baradarhan, S.; Moghaddam, E.; Basirun, W.; Mehrali, M.; Sookhakian, M.; Hamdi, M.; Moghaddam, M.; Alias, Y. Mechanical

properties and biomedical applications of a nanotube hydroxyapatite-reduced graphene oxide composite. *Carbon* **2014**, *69*, 32–45.

(10) Mehrali, M.; Moghaddam, E.; Shirazi, S. F. S.; Baradaran, S.; Mehrali, M.; Latibari, S. T.; Metselaar, H. S. C.; Kadri, N. A.; Zandi, K.; Osman, N. A. A. Synthesis, Mechanical Properties, and in Vitro Biocompatibility with Osteoblasts of Calcium Silicate–Reduced Graphene Oxide Composites. *ACS Appl. Mater. Interfaces* **2014**, *6*, 3947–3962.

(11) Sookhakian, M.; Amin, Y. M.; Basirun, W. J. Hierarchically ordered macro-mesoporous ZnS microsphere with reduced graphene oxide supporter for a highly efficient photodegradation of methylene blue. *Appl. Surf. Sci.* **2013**, *283*, 668–677.

(12) Basirun, W. J.; Sookhakian, M.; Baradaran, S.; Mahmoudian, M. R.; Ebadi, M. Solid-phase electrochemical reduction of graphene oxide films in alkaline solution. *Nanoscale Res. Lett.* **2013**, *8*, 1–9.

(13) Sookhakian, M.; Amin, Y.; Baradaran, S.; Tajabadi, M.; Golsheikh, A. M.; Basirun, W. A layer-by-layer assembled graphene/zinc sulfide/polypyrrole thin-film electrode via electrophoretic deposition for solar cells. *Thin Solid Films* **2014**, *552*, 204–211.

(14) Quintana, M.; Edvinsson, T.; Hagfeldt, A.; Boschloo, G. Comparison of dye-sensitized ZnO and TiO<sub>2</sub> solar cells: Studies of charge transport and carrier lifetime. *J. Phys. Chem. C* **2007**, *111*, 1035–1041.

(15) Ozasa, K.; Maeda, M.; Hara, M. Photoluminescence behavior of CdSe on GaAsO<sub>x</sub>/GaAs substrates. *Microelectron. J.* **2005**, *36*, 578–580.

(16) Mahmoudian, M. R.; Alias, Y.; Basirun, W. J. The electrical properties of a sandwich of electrodeposited polypyrrole nanofibers between two layers of reduced graphene oxide nanosheets. *Electrochim. Acta* **2012**, *72*, 53–60.

(17) Sookhakian, M.; Amin, Y. M.; Basirun, W. J.; Tajabadi, M. T.; Kamarulzaman, N. Synthesis, structural, and optical properties of type-II ZnO-ZnS core-shell nanostructure. *J. Lumin.* **2014**, *145*, 244–252.

(18) Ghosh Chaudhuri, R.; Paria, S. Core/shell nanoparticles: Classes, properties, synthesis mechanisms, characterization, and applications. *Chem. Rev. (Washington, DC, U.S.)* **2012**, *112*, 2373–2433.

(19) Gao, T.; Li, Q.; Wang, T. Sonochemical synthesis, optical properties, and electrical properties of core/shell-type ZnO nanorod/CdS nanoparticle composites. *Chem. Mater.* **2005**, *17*, 887–892.

(20) Mikhnenko, O. V.; Azimi, H.; Scharber, M.; Morana, M.; Blom, P. W. M.; Loi, M. A. Exciton diffusion length in narrow bandgap polymers. *Energy Environ. Sci.* **2012**, *5*, 6960–6965.

(21) Chen, C. P.; Chan, S. H.; Chao, T. C.; Ting, C.; Ko, B. T. Low-bandgap poly(thiophene-phenylene-thiophene) derivatives with broaden absorption spectra for use in high-performance bulk-heterojunction polymer solar cells. *J. Am. Chem. Soc.* **2008**, *130*, 12828–12833.

(22) Krauss, T. D.; Wise, F. W. Femtosecond measurement of nonlinear absorption and refraction in CdS, ZnSe, and ZnS. *Appl. Phys. Lett.* **1994**, *65*, 1739–1741.

(23) Muth, J. F.; Kolbas, R. M.; Sharma, A. K.; Oktyabrsky, S.; Narayan, J. Excitonic structure and absorption coefficient measurements of ZnO single crystal epitaxial films deposited by pulsed laser deposition. *J. Appl. Phys.* **1999**, *85*, 7884–7887.

(24) Ma, H.-L.; Zhang, H.-B.; Li, X.; Zhi, X.; Liao, Y.-F.; Yu, Z.-Z. The effect of surface chemistry of graphene on cellular structures and electrical properties of polycarbonate nanocomposite foams. *Ind. Eng. Chem. Res.* **2014**, *53*, 4697–4703.

(25) Dodoo-Arhin, D.; Fabiane, M.; Bello, A.; Manyala, N. Graphene: Synthesis, Transfer, and Characterization for Dye-Sensitized Solar Cells Applications. *Ind. Eng. Chem. Res.* **2013**, *52*, 14160–14168.